

Oxygen Reduction on Platinum

A thesis submitted for the degree of Doctor of Philosophy
in Physical and Theoretical Chemistry

Matthew Gara

St. John's College

2013

"Self citation is like masturbation: Accepted in small quantities, but too much and you're just a wanker."

2008

Abstract

Proton exchange membrane (PEM) fuel cells have the potential to provide a clean and convenient source of power for applications such as vehicle transport. At their heart lies a platinum catalyst which is used to reduce oxygen to water. Although platinum is expensive it is the best elemental catalyst for the reaction. In order to make better use of the platinum and reduce production costs, nanoparticulate platinum is dispersed onto a carbon support. This results in a greater surface area per gram of platinum used. Efforts to improve the performance of fuel cells and make them cost effective have so far revolved around increasing the surface area. However in doing this the inter-particle spacing and diffusional characteristics of the catalyst have been ignored.

In order to address this oversight, this thesis takes a novel bottom up approach to better understanding the oxygen reduction reaction on nanoparticulate platinum, supported on carbon. By using a model system and simulating the diffusional environment, this work reveals new insights into the oxygen reduction reaction.

In Chapter 1 the fundamental electrochemical principles which underpin the subsequent work shall are examined. Chapter 2 begins with a look at the history of fuel cell development, before assessing the modern PEM fuel cell and the challenges faced in the present day to make it a viable power source.

In Chapter 3 carbon electrode materials are assessed with a view towards their use as a substrate for platinum catalysts. The results gained from this prove useful in later chapters and are both novel and insightful for the selection of PEM fuel cell catalyst supports.

In Chapters 4 and 5 voltammetry at nanomaterial modified electrodes are extensively analysed, using electrochemical simulation techniques. This reveals that diffusion can play a role in effects which are assumed to be purely kinetic. From this a major flaw is exposed in the currently accepted measures of oxygen reduction catalyst activity.

Chapter 6 brings the information garnered from the previous chapters together. In this chapter nanoparticulate platinum dispersed onto a flat carbon substrate is used as a model system of a typical oxygen reduction catalyst. The resulting voltammetry from the

model surfaces is then fitted effectively to results from electrochemical simulations, paying close attention to the diffusional environment around the nanoparticles. This approach leads to a key finding which had hitherto gone unrecognised.

List of Tables

1.1 Potentials, relative to SHE, of a selection of common reference electrodes . 7

1.2 Randles-Ševčík equations for the four main categories of voltammetry, where I_p is the peak current, ν is the scan rate, $[O^x]_{bulk}$ is the bulk concentration of the species of interest, A is the geometric area of the electrode, D is the diffusion coefficient, T is the temperature, α is the transfer coefficient, n is the number of electrons transferred in the reaction and n' the number of electrons transferred before the rate determining electron transfer. 26

2.1 Comparison of major types of fuel cell. 45

5.1 Examples of fixed potentials used in the literature to compare platinum oxygen reduction catalysts. 121

5.2 Relationship between coverage and electroactive surface area where N is the total number of particles on the substrate, r is the radius of the particle in question, h is the height dimension for cylinders, l is the length dimension for wires and A is the geometric area of the electrode 126

5.3 Percentage difference in current density with respect to the total electroactive surface area (j) compared to surface coverage for arrays of hemispherical particles 134

5.4 Percentage difference in current density with respect to the total electroactive surface area (j) compared to surface coverage for arrays of spherical particles 136

5.5 Percentage difference in current density with respect to the total electroactive surface area (j) compared to surface coverage for arrays of hemicylindrical nanowires 137
5.6 % difference in j compared to surface coverage for arrays of cylinders 5 nm high and 10 nm in radius 142
5.7 % difference in j compared to cylinder radius for arrays of cylinders 5 nm high with a 40% coverage 143

6.1 Table summarising the three electrochemical mechanisms and their possible physical/chemical interpretations 166
6.2 Table summarising the fitted parameters used for the three different mechanisms across both low and high coverage. 175

List of Figures

1.1 Schematic showing the relative positions of the Fermi level when a) the conductor is first placed into solution and b) at equilibrium. Note how the equilibrated Fermi Level of the conductor resides *between* the Fermi levels of the two solvated species. 4

1.2 Diagram of a typical experimental implementation of an SHE reference electrode. This half cell is usually connected to the experimental cell by means of a porous frit, luggin capillary or salt-bridge. 6

1.3 Graph showing how the Gibbs energy of a reaction system changes as a reaction progresses to completion. Equilibrium is achieved when G_{sys} is at a minimum value. 8

1.4 Diagram showing the change in Gibbs energy with reaction coordinate. The forward and backward barriers to reach the transition state are labelled $\Delta G^{\ddagger}_{fwd}$ and $\Delta G^{\ddagger}_{bk}$ respectively. 12

1.5 Diagram showing how the Gibbs energy profile and transition-state barriers change with potential. The solid line on the reactants' side represents the profile when the potential is at E^0, the dotted line represents the profile when the potential is increased to a new value, E. 15

1.6 Plots of Gibbs energy profiles at different alpha values. Using alpha as an indicator of symmetry it can be seen that when α is less than 0.5 (c)) the transition state is product like and when α is more than 0.5 (a)) the transition state is reactant like. When $\alpha = 0.5$ the transition state exactly halfway between the two states. 17

1.7 A detailed view of the intersection of the Gibbs energy profiles in Figure 1.5 showing the angles which can be used to calculate α. 18
1.8 Diagram showing a hypothetical one-dimensional tube with the fluxes coming in and out of the section bounded by x and $x + dx$ labelled. 21
1.9 Plot showing how the concentration of $[O^x]$ increases linearly from the electrode surface until it reaches the value of the bulk solution concentration ($[O^x]_{bulk}$). The distance between x=0 and $x = \delta$ is the Nernst diffusion layer, δ. 22
1.10 Diagram showing the potential profile during a chronoamperometry experiment. The potential begins at starting potential (E_1) before jumping to another potential (E_2) for a set amount of time before returning to the original potential, E_1. 23
1.11 Diagram showing the potential profile during a cyclic voltammetry experiment. The potential begins at starting potential (E_i) before increasing at a linear rate (ν) until the vertex potential E_v is reached. The potential sweep then reverses until the final potential (E_f) is reached. 24
1.12 A typical cyclic voltammogram, starting at positive potential and scanning negative (cathodic scan) before sweeping in the opposite direction (anodic scan). The cathodic and anodic peak currents are labelled accordingly. . . 25
1.13 A flat planar macroelectrode in three dimensions. It is possible to simplify the problem of simulating this to just one-dimension so that only the z-axis is of importance. 28
1.14 A schematic of the final simplified model in one-dimension showing the sampling points as black dots. Note how the points cluster towards the electrode surface, as greater accuracy is required in this region. 30
1.15 Schematic diagram showing the application of the diffusion domain approximation to the problem of simulating an array of micro-disc electrodes. Using this method it is possible to simplify the original three-dimensional problem (a) into a two-dimensional problem. 32

1.16 Schematic diagram of the final two-dimensional simulation space showing the outer boundaries and sampling points (•). 33

2.1 The diagram from Grove's 1842 paper on the 'gaseous voltaic battery' showing four cells (similar to those he discovered in 1839) in sequence. The smaller cell to the top of the picture is an electrolytic cell to electrolyse water. Note, being pre-1897, the arrows indicating current flow are in, what might today be described as, the conventional direction not the direction of electron flow. 40

2.2 Photographs of the PEM fuel cell used on the Gemini space program. On the left is a cut-through demonstration model of the fuel cell showing one of its three fuel cell stacks. On the Right is the fuel cell installed on the command module. Images courtesy of NASA. 41

2.3 Images of the alkaline fuel cell used on the Apollo space program. On the left is a photograph of the alkaline fuel cell rack installed in the side of the Apollo service module. The diagram on the right shows the positioning of the fuel cells within the service module, other labels have been removed for clarity. Images courtesy of NASA. 42

2.4 Diagram of a general fuel cell. 43

2.5 Diagram of a proton exchange membrane (PEM)fuel cell. Hydrogen gas is oxidised on the anode splitting into protons and electrons, the protons pass through the membrane to the cathode, the electrons flow around an electrical circuit (producing a current) to the cathode where oxygen is reduced to water, using the afore mentioned protons as a proton source. . . 44

2.6 Diagram of a proton exchange membrane (PEM)fuel cell stack. The black crenelated sections are termed bi-polar plates and feed hydrogen on one side and oxygen on the other. Note, the gas diffusion layer from Figure 2.5 has been omitted for clarity. 47

2.7 Graph showing the historical price of platinum, from 1992. Data from Johnson Matthey 50

3.1 Structure of Nafion® 58
3.2 Structure of graphite illustrating the relative orientations of the of the basal and edge planes 60
3.3 Extract from reference 17 showing the structure of glassy carbon. 61
3.4 The structures of different multiwalled carbon nanotubes. a) Hollow multiwalled carbon nanotubes (H-MWCNT). b) Bamboo multiwalled carbon nanotubes (B-MWCNT). Note the positions and frequency of the edge planes. 61
3.5 Cyclic voltammograms performed using a BDD electrode, comparing data acquired in O_2 saturated (╲) and N_2 saturated (˙··) H_2SO_4 taken at scan rates of a) 10 mV s^{-1}, b) 20 mV s^{-1}, c) 40 mV s^{-1}, d) 100 mV s^{-1}, e) 200 mV s^{-1}, f) 400 mV s^{-1} and g) 800 mV s^{-1}. Note the voltammetric traces crossing and unconventional capacitive response due to bubble formation on the electrode at extreme negative potentials. 65
3.6 Cyclic voltammograms performed using a glassy carbon electrode, comparing data acquired in O_2 saturated (╲) and N_2 saturated (˙··) H_2SO_4 taken at scan rates of a) 10 mV s^{-1}, b) 20 mV s^{-1}, c) 40 mV s^{-1}, d) 100 mV s^{-1}, e) 200 mV s^{-1}, f) 400 mV s^{-1} and g) 800 mV s^{-1} 67
3.7 Cyclic voltammograms performed using a BPPG electrode, comparing data acquired in O_2 saturated (╲) and N_2 saturated (˙··) H_2SO_4 taken at scan rates of a) 10 mV s^{-1}, b) 20 mV s^{-1}, c) 40 mV s^{-1}, d) 100 mV s^{-1}, e) 200 mV s^{-1}, f) 400 mV s^{-1} and g) 800 mV s^{-1} 68
3.8 Cyclic voltammograms performed using a EPPG electrode, comparing data acquired in O_2 saturated (╲) and N_2 saturated (˙··) H_2SO_4 taken at scan rates of a) 10 mV s^{-1}, b) 20 mV s^{-1}, c) 40 mV s^{-1}, d) 100 mV s^{-1}, e) 200 mV s^{-1}, f) 400 mV s^{-1} and g) 800 mV s^{-1} 69
3.9 A Randles-Ševčík plot (*c.f.* equation (3.12)) of the peak currents from Figure 3.8 giving a gradient of -4.41x10^{-4} with $R^2 = 0.999$ 70

3.10 An example of Tafel analysis with a line of best fit going through the Tafel region of the voltammogram. The gradient of the tafel region, in this particular case, was found to be -14.62. 71

3.11 Cyclic voltammograms performed using a SWCNT modified BPPG electrode, comparing data acquired in O_2 saturated (╲) and N_2 saturated (˙·.) H_2SO_4 taken at scan rates of a) 10 mV s^{-1}, b) 20 mV s^{-1}, c) 40 mV s^{-1}, d) 100 mV s^{-1}, e) 200 mV s^{-1}, f) 400 mV s^{-1} and g) 800 mV s^{-1} 72

3.12 Cyclic voltammograms performed using a B-MWCNT modified BPPG electrode, comparing data acquired in O_2 saturated (╲) and N_2 saturated (˙·.) H_2SO_4 taken at scan rates of a) 10 mV s^{-1}, b) 20 mV s^{-1}, c) 40 mV s^{-1}, d) 100 mV s^{-1}, e) 200 mV s^{-1}, f) 400 mV s^{-1} and g) 800 mV s^{-1} 73

3.13 Cyclic voltammograms performed using a H-MWCNT modified BPPG electrode, comparing data acquired in O_2 saturated (╲) and N_2 saturated (˙·.) H_2SO_4 taken at scan rates of a) 10 mV s^{-1}, b) 20 mV s^{-1}, c) 40 mV s^{-1}, d) 100 mV s^{-1}, e) 200 mV s^{-1}, f) 400 mV s^{-1} and g) 800 mV s^{-1} 74

3.14 Further analysis of the results acquired from the H-MWCNT modified electrode. a) A log current vs. log scan rate plot showing theoretical results (• and ˙·.) giving a gradient of 0.5 with $R^2 = 1$ and analysable experimental results (■ and ╲) giving a gradient of 0.63 with $R^2 = 0.997$. b) A plot of the 'residual' current from subtracting the theoretical from experimental results shown in a) with a linear fit giving a gradient of -3.06x10^{-4} and $R^2 = 0.997$. Note the excellent agreement with the linear fit. 75

3.15 Collation of 400 mV s^{-1} scans, taken in O_2 saturated H_2SO_4 carbon nanotube modified BPPG electrodes. B-MWCNT - red, SWCNT - Blue, H-MWCNT - Green and the underling BPPG support - Black. The signal for glassy carbon has been corrected (according to equation (3.12) so as to account for the difference in geometric electrode area) 77

3.16 Collation of 400 mV s^{-1} scans taken with macro electrodes. EPPG - green, GC - Red, BPPG - black and BDD - Blue 78

4.1 a) Variation of peak current density with standard electrochemical rate constant (k^0) b) Variation of peak potential (relative to the formal potential, E_f^0) with the standard electrochemical rate constant, k^0 87

4.2 Schematic diagrams of the four diffusional cases for an array of microelectrodes, complete with an expected voltammetric response for the type of behaviour represented. a) Case 1 b) Case 2 c) Case 3 and d) Case 4 88

4.3 Schematic diagrams for the range of electrode morphologies used. Black reas depict elctrochemically inactive areas whilst yellow areas depict electrochemically active areas. a) Planar, flat macroelectrode, b) array of microdiscs embedded in an electrochemically inactive substrate, c) array of electrochemically active hemispheres on an inactive substrate, d) array of electrochemically active hemispheres on an active substrate, e) array of electrochemically active spheres on an inactive substrate, f) a series of long, electrochemically active, hemicylindrical wires on an inactive substrate and g) array of active cylindrical particles places perpendicular to an inactive substrate. 91

4.4 Voltammetry of an array of hemispherical nanoparticles with varying rate constant, k^0, in the range 10^{-1}, 10^{-2}, 10^{-3}, ..., 10^{-9}, 10^{-10}, $\Theta = 0.5$, $r = 100$ nm, $d = 282$ nm, $[\mathrm{A}]_{bulk} = 1$ mM, $D = 10^{-5}$ cm^2 s^{-1}, $\alpha = 0.5$ and $\nu = 0.1$ V s^{-1} 93

4.5 Voltammetry of an array of hemispherical nanoparticles as it varies with surface coverage, Θ, in increments of 0.1. $k = 10^{-7}$ cm s^{-1}, $r = 100$ nm, $[\mathrm{A}]_{bulk} = 1$ mM, $D = 10^{-5}$ cm^2 s^{-1}, $\alpha = 0.5$ and $\nu = 0.1$ V s^{-1} 94

4.6 Variation of peak potential, E_p, with coverage, Θ, for a range of values of rate constant, k^0, for an array of hemispherical particles with $r = 100$ nm, $[\mathrm{A}]_{bulk} = 1$ mM, $D = 10^{-5}$ cm^2 s^{-1}, $\alpha = 0.5$, $\nu = 0.1$ V s^{-1} 95

4.7 Summarised data from simulation of arrays of hemispheres at various coverages using $k^0 = 10^{-7}$ cm s^{-1}, r = 100 nm, [A] = 1 mM, D = 10^{-5} cm^2, s^{-1}, $\alpha = 0.5$, $\nu = 0.1$ V s^{-1}. a) Peak current (I_p) as a function of the irreversible Randles-Ševčík limit (I_{RS}) from equation (4.3) plotted as function of ln Ψ . b) Peak potential (E_p), relative to formal potential (E_f^0), plotted as a function of ln Ψ 98

4.8 Voltammetry of an array of hemispherical nanoparticles as it varies with surface coverage, Θ, in increments of 0.1. $k = 10^{-3}$ cm s^{-1}, $r_e = 100$ nm, $[A]_{bulk} = 1$ mM, $D = 10^{-5}$ cm^2 s^{-1}, $\alpha = 0.5$, $\nu = 0.1$ V s^{-1} 99

4.9 a) Simulated voltammetry of an array of hemispherical nanoparticles with varying transfer coefficient (α) from 0.2 - 0.8. The dashed line shows the peak position for varying α, in terms of E_p and I_p when predicted by Equations 4.18 and 4.3 respectively. b) A plot of $\alpha(E_p - E_f^0)$ against ln ($\alpha^{1/2}$) using the simulated data from a). The dashed line shows the values predicted by Equation 4.20. With $\Psi = 0.6$, $k = 10^{-7}$ cm s^{-1}, $r = 100$ nm, $[A]_{bulk} = 1$ mM, $D = 10^{-5}$ cm^2 s^{-1}, $\alpha = 0.5$, $\nu = 0.1$ V s^{-1} 100

4.10 Variation of E_p with scan rate, ν, in the range $10^{-4} - 10^4$ V s^{-1}, for an array of hemispherical particles with $\Psi = 0.6$, $k = 10^{-7}$ cm s^{-1}, $r_e = 100$ nm , $d = 365$ nm, $[A]_{bulk} = 1$ mM, $D = 10^{-5}$ cm^2 s^{-1}, $\alpha = 0.5$ 101

4.11 Variation of a) peak potential, and b) peak current with particle radius, r, for a range of values of Ψ, for an array of hemispherical particles with $k^0 = 10^{-7}$ cm s^{-1}. Dashed horizontal lines in (a) show the value predicted by Equation 4.18. c) shows the variation of I_p with Ψ for $r = 10^{-5}$ m. Other parameters are kept constant with $[A]_{bulk} = 1$ mM, $D = 10^{-5}$ cm^2 s^{-1}, $\alpha = 0.5$, $\nu = 0.1$ V s^{-1} 103

4.12 simulated voltammetry for an array of electrochemically active hemispheres atop an electrochemically active substrate where $[A]_{bulk} = 1$ mM $D = 10^{-5}$ cm^2 s^{-1} $\alpha = 0.5$ $\nu = 0.1$ V s^{-1}, $r = 100$ nm . a) Variation of standard electrochemical rate constant, k^0, from 10^{-1} to 10^{-9} in factors of 10 ($\Theta = 0.5$ ($\Psi = 1.5$)). b) Voltammetry of an array of hemispherical particles on an active surface as it varies with surface coverage, Θ, in increments of 0.1. $k^0 = 10^{-7}$ cm s^{-1}. c) Variation of peak potential, E_p, with coverage, Θ, for a range of values of electrochemical rate constant, k^0. Dotted lines show values predicted by Equation 4.18. 104

4.13 simulated voltammetry for an array of electrochemically active spheres atop an electrochemically in active substrate where $[A]_{bulk} = 1$ mM $D = 10^{-5}$ cm^2 s^{-1} $\alpha = 0.5$ $\nu = 0.1$ V s^{-1}, $r = 100$ nm . a) Variation of standard electrochemical rate constant, k^0, from 10^{-1} to 10^{-9} in factors of 10 ($\Theta = 0.5$ ($\Psi = 1.5$)). b) Voltammetry of an array of spherical particles on an inactive surface as it varies with surface coverage, Θ, in increments of 0.1. $k^0 = 10^{-7}$ cm s^{-1}. c) Variation of peak potential, E_p, with coverage, Θ, for a range of values of electrochemical rate constant, k^0. Dotted lines show values predicted by Equation 4.18. 106

4.14 simulated voltammetry results from simulations on an array of long, electrochemically active, hemicylindrical wires on top of an electrochemically inactive substrate where $[A]_{bulk} = 1$ mM $D = 10^{-5}$ cm^2 s^{-1} $\alpha = 0.5$ $\nu = 0.1$ V s^{-1}, $r = 100$ nm . a) Variation of standard electrochemical rate constant, k^0, from 10^{-1} to 10^{-9} in factors of 10 ($\Theta = 0.5$ ($\Psi = 1.5$)). b) Voltammetry of an array of electroactive hemicylindrical wires on top of an inactive substrate as it varies with surface coverage, Θ, in increments of 0.1 ($k^0 = 10^{-7}$ cm s^{-1}). c) Variation of peak potential, E_p, with coverage, Θ, for a range of values of electrochemical rate constant, k^0. Dotted lines show values predicted by Equation 4.18. 107

4.15 Results arising for simulations of electrochemically active cylinders atop an electrochemically inactive substrate.$[A]_{bulk} = 1$ mM, $D = 10^{-5}$ cm^2 s^{-1}, $\alpha = 0.5$, $\nu = 0.1$ V s^{-1}. a) Variation of surface coverage, Θ, in increments of 0.2. $k^0 = 10^{-6}$ cm s^{-1} and $r = h = 100$ nm. b) Variation with cylinder height, h, in increments of 20 nm. $k = 10^{-6}$ cm s^{-1}, $\Theta = 0.5$, $r = 100$ nm . c) Variation of peak potential, E_p, with coverage, Θ, for a range of values of cylinder height, h, with $r = 100$ nm, $k^0 = 10^{-6}$ cm s^{-1} 109

4.16 Voltammetry (at two different scales) of two systems with the same mass of electroactive material divided into spherical particles: 'A' has N particles with $r = 100$ nm and $\Psi = 0.4$; 'B' has $2N$ particles with $r = 79.4$ nm and $\Psi = 0.504$. The difference in peak potential between the two is $\Delta E_{\mathrm{p}} = 11.9$ mV. Other parameters: $k^0 = 10^{-7}$ cm s^{-1}, $\nu = 0.1$ V s^{-1}, $[A]_{bulk} = 1$ mM, $D = 10^{-5}$ cm^2 s^{-1}, $\alpha = 0.5$. 112

5.1 The four general diffusional cases for a nanoparticle modified electrode. a) Case 1. b) Case 2. c) Case 3. d) Case 4. 122

5.2 Simulated voltammograms for hemispherical nanoparticle modified electrodes, of varying coverages (10, 20, 30 , 40, 50, 60, 70%) in terms of: a) current b) current density with respect to the total electroactive surface area. The inset for each graph shows the region around 900mV. 128

5.3 Simulated voltammograms for hemispherical nanoparticle modified electrodes, of varying sizes (5, 10, 20, 50, 100 nm in radius) in terms of: a) current b) current density with respect to the total electroactive surface area. The inset for each graph shows the region around 900mV. 129

5.4 Simulated voltammograms for spherical nanoparticle modified electrodes, of varying a) coverages (10, 20, 30 , 40, 50, 60, 70%) and b) sizes (20, 50, 100 nm in radius) as a function of current density with respect to the total electroactive surface area. The inset for each graph shows the region around 900mV. 131

5.5 Simulated voltammograms for nanowire modified electrodes, of varying a) coverages (10, 20, 30 , 40, 50, 60, 70%) and b) sizes (5, 10, 20, 50, 100 nm in radius) as a function of current density with respect to the total electroactive surface area. The inset for each graph shows the region around 900mV. 132

5.6 Graph showing the percentage difference in the current density with respect to the total electroactive surface area associated with taking the current density at 900, 850 and 800 mV for an array of hemispherical particles. The percentage difference is taken relative to the value at 10% 133

5.7 Graph showing the percentage error in the current density associated with taking the current density with respect to the total electroactive surface area at 900, 850 and 800mV for arrays of a)spherical particles and b)nanowires. The percentage difference is taken relative to the value at 10% 135

5.8 Simulated voltammograms for an array of cylinders 5 nm high and 10 nm in radius, of varying coverages (10, 20, 30 , 40, 50, 60, 70%) in terms of: a) current b) current density with respect to the total electroactive surface area. The inset for each graph shows the region around 900mV. 139

5.9 Simulated voltammograms for arrays of cylinders 5 nm high of varying radii (5, 10, 20, 50, 100 nm in radius) at a constant 40% coverage ($N\pi r^2$) as a function of: a) current b) current density with respect to the total electroactive surface area. The inset for each graph shows the region around 900mV. 140

5.10 Graph showing the percentage difference in the current density associated with taking the current density at 900, 850 and 800mV for an array of cylinders. a)Taken for arrays of cylinders 5 nm high and 10 nm in radius across a range of coverages and b) taken for arrays of cylinders 5 nm high of varying radii at a constant 40% coverage. 141

6.1 Schematic illustrating the two possible scenarios in a stepwise oxygen reduction reaction in acid. a)The two electron reduction of O_2 to H_2O_2 followed by diffusion of H_2O_2 in to solution. b)The two electron reduction of O_2 to H_2O_2 followed by a further two electron reduction to H_2O 152

6.2 a) Voltammetric response of glassy carbon in 1 mM H_2PtCl_6 with 0.5M $H_2SO_{4\ (aq)}$ from 0.94 to -0.160 V starting with the cathodic sweep. The peaks corresponding to the reductions of $Pt_{(IV)}$ and $Pt_{(II)}$ and the responses for H^+ reduction and H_2 oxidation on the freshly deposited platinum are labelled accordingly. b) A more detailed view of the region between 0.6 and -0.05 V. 156

6.3 The pretreatment procedure used to prepare the glassy carbon deposition substrates. Glassy carbon electrodes were cycled from -0.05 to 1.3 V in N_2 saturated 0.5 M H_2SO_4 and back again for 20 cycles. The lightest grey line represents the 1^{st} cycle with the traces becoming gradually darker towards the 20^{th} cycle. Note how the voltammetric response slowly becomes more equable with each passing cycle. 157

6.4 The oxygen reduction response of the pretreated 'blank' glassy carbon substrate *before* electrodeposition of platinum nanoparticles. The solid line (╲) shows the trace for the substrate used for 30 s deposition and dashed line (˙˙·) for 15 s deposition. Note how no appreciable signal is seen before 0.15 V 157

6.5 Chronoamperograms for the glassy carbon substrates taken in N_2 saturated 1 mM H_2PtCl_6 with 0.5 M H_2SO_4 taken for 30 s (╲) and 15 s (˙˙·). 158

6.6 Cyclic voltammetry obtained of Pt nanoparticle array samples performed in O_2 saturated 0.5 M $H_2SO_4$for the a) low coverage-small nanoparticle sample acquired using a 15 s deposition time and b) high coverage-large nanoparticle sample acquired using a 30 s deposition time. Black - 10 mV s^{-1}, red - 20 mV s^{-1}, blue - 40 mV s^{-1}, pink - 80 mV s^{-1}, green - 160 mV s^{-1}, indigo - 320 mV s^{-1}, violet - 640 mV s^{-1}. 159

6.7 Randles-Ševčík plot of the cyclic voltammetry data for both low (•) and high (▲) coverage samples. Solid (╲) and dashed (˙·.) show the theoretical Randles-Ševčík values, for a uniformly active, flat electrode using alpha values of 0.4 (attained for the high coverage case) and 0.3 (low coverage case) respectively, for both 2 and 4 electron cases (as indicated). The rough α values used were obtained from simple Tafel analysis rather than fitting. 160

6.8 a)-c) SEM images at increasing magnification acquired for the low coverage-small nanoparticle sample. Image b) along with others of the same magnification were used to calculate a coverage of 0.46%, with standard deviation 0.10%. d) Histogram made by taking measurements from images akin to c) giving an average particle radius of 29 nm with standard deviation 11.4 nm. The solid black trace shows the corresponding Gaussian fit of the particle size data, with no offset, giving a FWHM of 30.9 nm. 162

6.9 a)-c) SEM images at increasing magnification acquired for the High coverage-large nanoparticle sample. Image b) along with others of the same magnification were used to calculate a coverage of 1.96%, with standard deviation 0.42% d)Histogram made by taking measurements from images akin to c) giving an average particle radius of 136 nm, with standard deviation 52.8 nm. The solid black trace shows the corresponding Gaussian fit of the particle size data, with no offset, giving a FWHM of 115.0 nm. 163

6.10 Comparison of an experimental voltammograms (╲) against simulated voltammograms (˙·.) obtained using an EE mechanism. a) 20 mV s^{-1} b) 320 mV s^{-1}. 168

6.11 Randles-Ševčík plot of the experimental (■) and simulated (□) voltammograms, using an EE mechanism. Note the good fit obtained in all but the very lowest scan rates despite this being only a two electron mechanism. . 169

6.12 A plot of the effective number of electrons transferred per O_2 molecule (calculated from the current) vs. log k^c_{het} showing the transition from 2 electrons to 4 electrons depending on the rate constant of the intermediate, chemical step ('C' step). 170

6.13 Comparison of experimental voltammograms (╲) against simulated voltammograms (˙·.) obtained using an EECEE mechanism. a) 20 mV s^{-1} low coverage-small nanoparticle, b) 320 mV s^{-1} low coverage-small nanoparticle, c) 20 mV s^{-1} high coverage-large nanoparticle and d) 320 mV s^{-1} high coverage-large nanoparticle 171

6.14 Randles-Ševčík plot of the experimental (■) and simulated (□) voltammograms, using an EECEE mechanism, for both a)the high coverage-large nanoparticle case and b)the low coverage-small nanoparticle case. The solid lines represent the simple 2 and 4 electron reduction boundaries calculated by simulation of a sequential EE and EEEE mechanisms respectively for the same nanoparticle size and coverage as that being investigated. D, $[O_2]_{bulk}$ parameters are kept constant throughout. 172

6.15 Comparison of experimental voltammograms (╲) against simulated voltammograms (˙·.) obtained using an EEC_{cyc} mechanism. a) 20 mV s^{-1} low coverage-small nanoparticle, b) 320 mV s^{-1}low coverage-small nanoparticle, c) 20 mV s^{-1} high coverage-large nanoparticle and d) 320 mV s^{-1} high coverage-large nanoparticle 173

6.16 Randles-Ševčík plot of the experimental (■) and simulated (□) voltammograms, using an EEC_{cyc} mechanism, for both a)the high coverage-large nanoparticle case and b)the low coverage-small nanoparticle case. The solid lines represent the simple 2 and 4 electron reduction boundaries calculated by simulation of a sequential EE and EEEE mechanisms respectively for the same nanoparticle size and coverage as that being investigated. D, $[O_2]_{bulk}$ parameters are kept constant throughout. 174

7.1 Scheme showing the two competing modes of oxygen reduction at nanoparticulate platinum. In the first, the oxygen undergoes two-electron reduction to form hydrogen peroxide before the peroxide diffuses away. In the second, the hydrogen peroxide undergoes a further two-electron reduction to form water, giving an overall four-electron reduction. Which mode dominates is entirely dependent on the mass transport conditions. 184
7.2 Diagram of a car with a fuel cell wired directly to a motor. 185
7.3 Diagram of a hybrid fuel cell powered vehicle. In this configuration the motor is powered by a battery which is being charged by a fuel cell. 186

A.1 Simulated voltammograms for hemispherical nanoparticle modified electrodes, of varying sizes (5, 10, 20, 50, 100 nm in radius) in terms of current density, with respect to the total electroactive surface area, for fixed coverages of a) 20% and b)60%. The inset for each graph shows the region around 900mV. 189
A.2 Simulated voltammograms for spherical nanoparticle modified electrodes, of varying sizes (20, 50, 100 nm in radius) in terms of current density, with respect to the total electroactive surface area, for fixed coverages of a) 20% and b)60%. The inset for each graph shows the region around 900mV. . . . 190
A.3 Simulated voltammograms for semicircular nanowire modified electrodes, of varying sizes (5, 10, 20, 50, 100 nm in radius) in terms of current density, with respect to the total electroactive surface area, for fixed coverages of a) 20% and b)60%. The inset for each graph shows the region around 900mV. 191

B.1 Voltammograms using a nanoparticle array with a 15s deposition time, taken in O_2 saturated 0.5 M H_2SO_4 (soild) and N_2 saturated 0.5 M H_2SO_4 (dashed). 193
B.2 Voltammograms using a nanoparticle array with a 30s deposition time, taken in O_2 saturated 0.5 M H_2SO_4 (soild) and N_2 saturated 0.5 M H_2SO_4 (dashed). 194

Contents

1 Introduction: Electrochemical Principles **1**

1.1 Origins of Electrochemical Potential . . . 3
1.2 Measuring the Electrochemical Potential and Reference electrodes . . . 4
1.2.1 Standard Hydrogen Electrode (SHE) . . . 5
1.2.2 Other Reference electrodes . . . 6
1.3 The Nernst Equation . . . 7
1.3.1 The Effect of pH . . . 10
1.4 Electrode Kinetics . . . 11
1.4.1 The Transfer Coefficient (α) . . . 17
1.4.2 Tafel Analysis . . . 18
1.5 Diffusion . . . 19
1.5.1 Fick's Laws . . . 20
1.5.2 Nernst Diffusion Layer . . . 21
1.6 Experimental Techniques . . . 23
1.6.1 Chronoamperometry . . . 23
1.6.2 Voltammetry . . . 24
1.7 Strategies for Simulating Voltammetry . . . 27
1.7.1 Voltammetry at a Planar Electrode (1D Simulation) . . . 28
1.7.2 Voltammetry at an Array of Microdiscs (2D Simulation) . . . 31
Bibliography . . . 36

2 Introduction: Fuel Cells **38**

2.1 History of Fuel Cells . . . 39
2.2 Types of Fuel Cell . . . 43
2.3 The Proton Exchange Membrane Fuel Cell . . . 44
2.3.1 Problems with PEM fuel cells . . . 48
2.4 Aims . . . 51
Bibliography . . . 52

3 Oxygen Reduction on Carbon in Dilute Sulphuric Acid **55**
3.1 Aims . . . 56
3.2 Introduction . . . 56
3.3 Types of Carbon Electrode Materials . . . 59
3.4 Experimental Methods . . . 62
3.5 Results and Discussion . . . 63
3.5.1 Carbon Macroelectrodes . . . 63
3.5.2 Carbon Nanotube Modified Electrodes . . . 71
3.6 Summary & Conclusion . . . 77
Bibliography . . . 80

4 Investigating Apparent Altered Electrode Kinetics for Non-Flat Electrodes **84**
4.1 Aims . . . 85
4.2 Introduction . . . 85
4.3 Simulations . . . 90
4.4 Results and Discussion . . . 92
4.4.1 Hemispheres . . . 93
4.4.2 Other Surface Morphologies . . . 105
4.5 Summary and Conclusions . . . 110
Bibliography . . . 113

5 Implications of Apparent Altered Electrode Kinetics: A Case Study for Oxygen Reduction Catalysts **118**
5.1 Introduction . . . 119
5.2 Theory . . . 120
5.3 Computational Methods . . . 125
5.4 Results and Discussion . . . 126
5.4.1 Hemispheres, Spheres and wires . . . 127
5.4.2 Cylinders . . . 130
5.5 Conclusions . . . 144
Bibliography . . . 145

6 Oxygen Reduction at Sparse Arrays of Platinum Nanoparticles in Aqueous Acid **150**
6.1 Aims . . . 151
6.2 Introduction . . . 151
6.3 Experimental . . . 153
6.3.1 Preparation of Platinum Nanoparticle Arrays . . . 154

6.3.2 Simulation 156
6.4 Results and Discussion 158
6.4.1 Cyclic Voltammetry 158
6.4.2 Platinum Nanoparticle Characterisation 161
6.4.3 Simulation and Fitting 162
6.5 Summary and Conclusions 175
Bibliography 177

7 Final Conclusions **182**
Bibliography 187

A **188**

B **192**

Appendix A

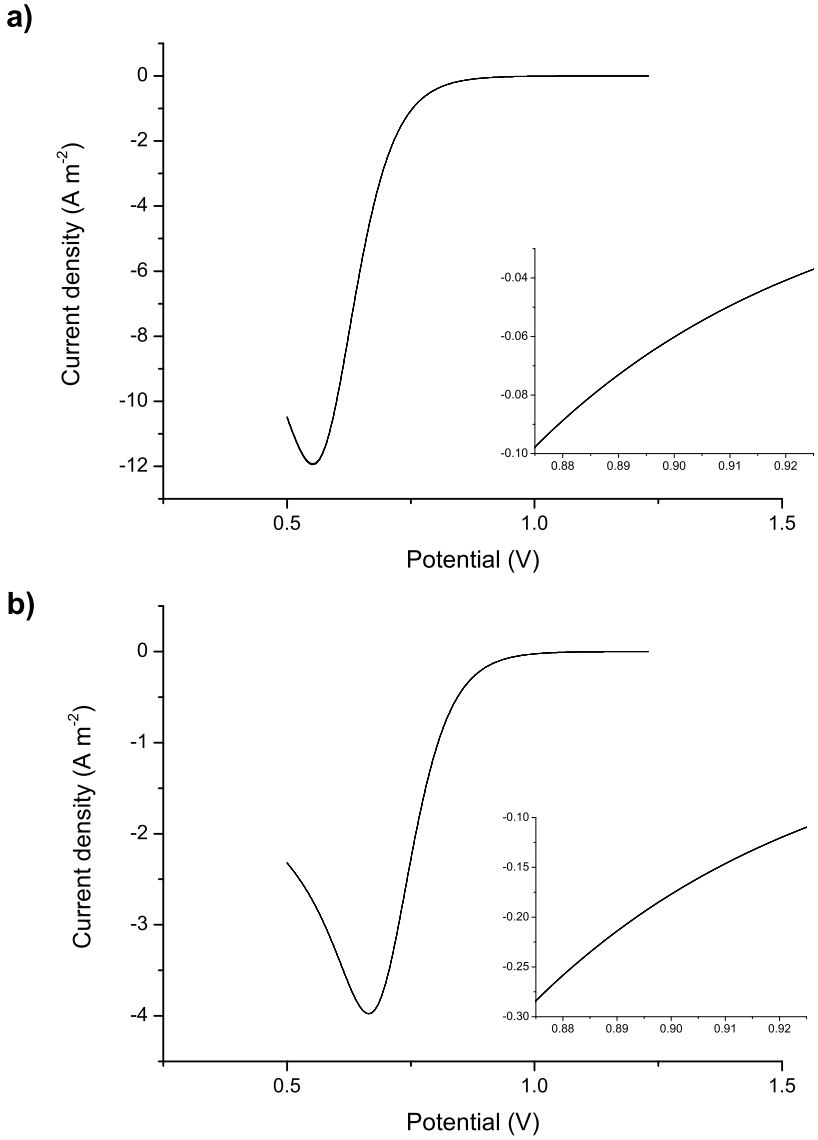


Figure A.1: Simulated voltammograms for hemispherical nanoparticle modified electrodes, of varying sizes (5, 10, 20, 50, 100 nm in radius) in terms of current density, with respect to the total electroactive surface area, for fixed coverages of a) 20% and b)60%. The inset for each graph shows the region around 900mV.

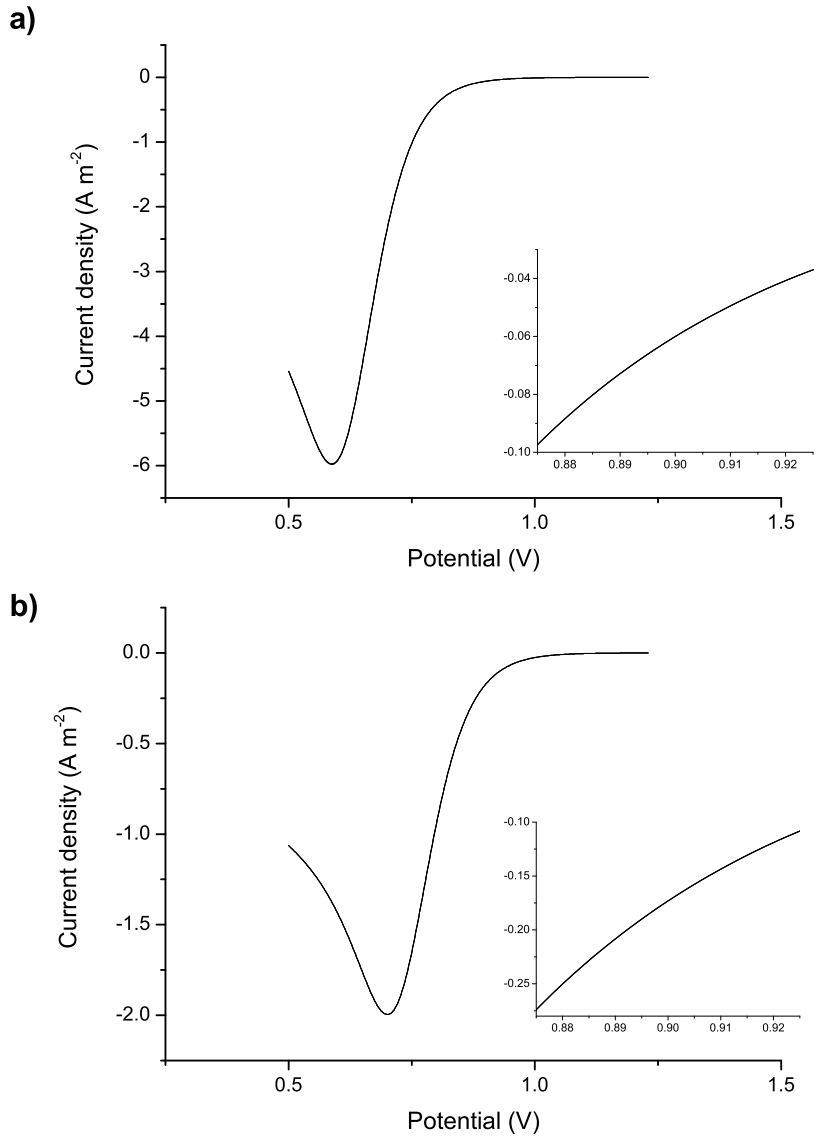


Figure A.2: Simulated voltammograms for spherical nanoparticle modified electrodes, of varying sizes (20, 50, 100 nm in radius) in terms of current density, with respect to the total electroactive surface area, for fixed coverages of a) 20% and b)60%. The inset for each graph shows the region around 900mV.

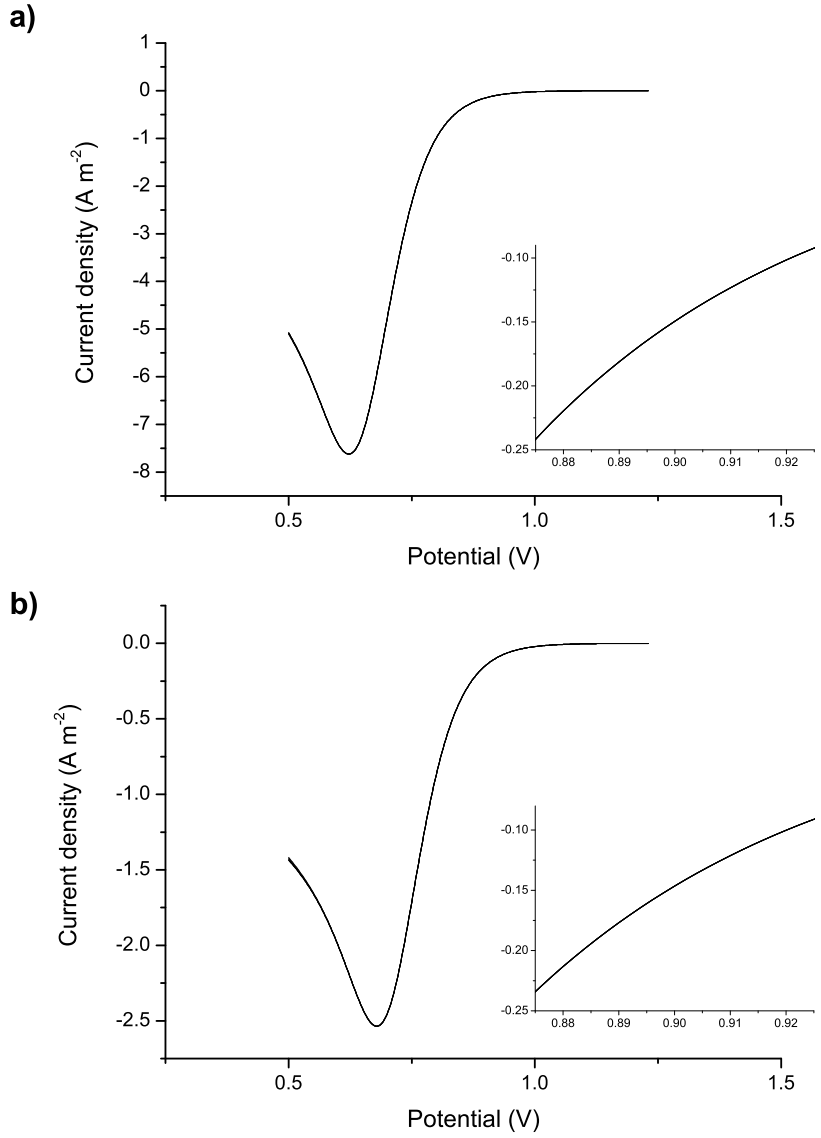


Figure A.3: Simulated voltammograms for semicircular nanowire modified electrodes, of varying sizes (5, 10, 20, 50, 100 nm in radius) in terms of current density, with respect to the total electroactive surface area, for fixed coverages of a) 20% and b)60%. The inset for each graph shows the region around 900mV.

Appendix B

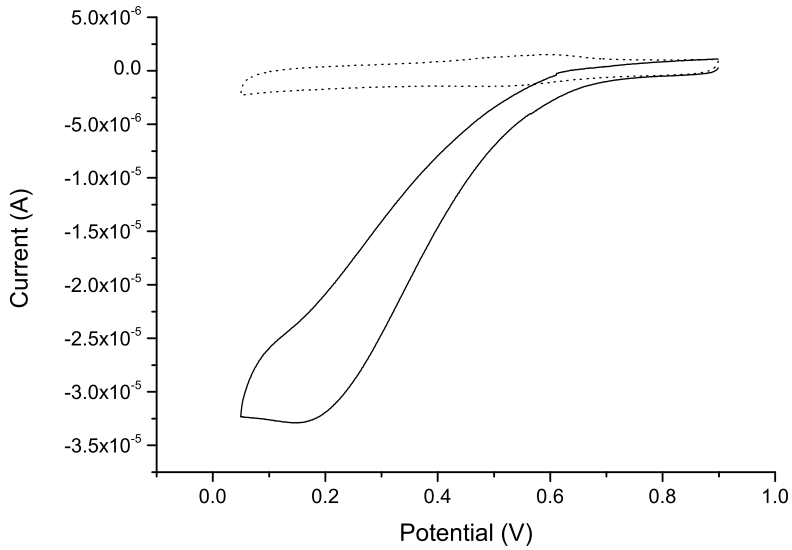


Figure B.1: Voltammograms using a nanoparticle array with a 15s deposition time, taken in O_2 saturated 0.5 M H_2SO_4 (soild) and N_2 saturated 0.5 M H_2SO_4 (dashed).

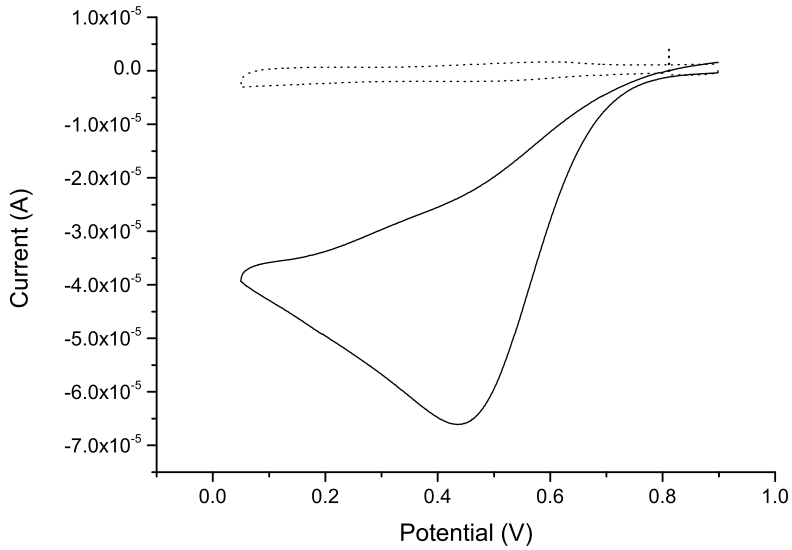


Figure B.2: Voltammograms using a nanoparticle array with a 30s deposition time, taken in O_2 saturated 0.5 M H_2SO_4 (soild) and N_2 saturated 0.5 M H_2SO_4 (dashed).